The Astrophysical Journal, 604:521–533, 2004 April 1

THE LUMINOSITY-SIZE AND MASS-SIZE RELATIONS OF GALAXIES OUT TO $z \sim 3$[1]

Ignacio Trujillo,[2] Gregory Rudnick,[3] Hans-Walter Rix,[2] Ivo Labbé,[4] Marijn Franx,[4] Emanuele Daddi,[5] Pieter G. van Dokkum,[6] Natascha M. Förster Schreiber,[4] Konrad Kuijken,[4] Alan Moorwood,[5] Huub Röttgering,[4] Arjen van de Wel,[4] Paul van der Werf,[4] and Lottie van Starkenburg[4]

Received 2003 July 1; accepted 2003 December 16

ABSTRACT

The luminosity-size and mass-size distributions of galaxies out to $z \sim 3$ are presented. We use very deep near-infrared images of the Hubble Deep Field–South in the J_s, H, and K_s bands, taken as part of FIRES at the VLT, to follow the evolution of the optical rest-frame sizes of galaxies. For a total of 168 galaxies with $K_{s,\mathrm{AB}} \leq 23.5$, we find that the rest-frame V-band sizes $r_{e,V}$ of luminous galaxies ($\langle L_V \rangle \sim 2 \times 10^{10}\ h^{-2}\ L_\odot$) at $2 < z < 3$ are 3 times smaller than for equally luminous galaxies today. In contrast, the mass-size relation has evolved relatively little: the size at mass $\langle M_* \rangle \sim 2 \times 10^{10}\ h^{-2}\ M_\odot$ has changed by 20% ($\pm$20%) since $z \sim 2.5$. Both results can be reconciled by the fact that the stellar M/L ratio is lower in the luminous high-z galaxies than in nearby ones because they have young stellar populations. The lower incidence of large galaxies at $z \sim 3$ seems to reflect the rarity of galaxies with high stellar mass.

Subject headings: galaxies: evolution — galaxies: fundamental parameters — galaxies: high-redshift — galaxies: structure — infrared: galaxies

On-line material: machine-readable table

1. INTRODUCTION

The size evolution of galaxies with redshift serves as an important constraint on models of galaxy evolution. In the current standard cosmology ($\Omega_M = 0.3$, $\Omega_\Lambda = 0.7$), hierarchical models of galaxy formation predict a strong increase in the characteristic size of galaxies since $z \sim 3$ (Baugh et al. 1998; Mao, Mo, & White 1998; Avila-Reese & Firmani 2001; Somerville, Primack, & Faber 2001). This, however, has not yet been extensively tested by observations. Early studies using ground-based telescopes (Smail et al. 1995) and the *Hubble Space Telescope* (*HST*; Casertano et al. 1995) showed that at magnitudes of $I \approx 22$ and $R \approx 26$, where the expected median redshift is greater than 0.5, the dominant field population is formed by very small systems with a mean scale length of $\sim$0.″2–0.″3. These objects are more compact than one would expect by assuming a fixed intrinsic physical size (Smail et al. 1995). Subsequent studies (Roche et al. 1998) at fainter magnitudes ($22 < I < 26$) suggested that most size evolution occurs at $z > 1.5$.

The study of galaxy properties at larger redshifts ($z > 2$) was dramatically improved by the identification of a large population of star-forming galaxies (Steidel et al. 1996). These Lyman break galaxies (LBGs) are identified by the redshifted break in the far-UV continuum caused by intervening and intrinsic neutral hydrogen absorption. Sizes of galaxies at $z \sim 3$ have been measured for LBGs (Giavalisco, Steidel, & Macchetto 1996; Lowenthal et al. 1997; Ferguson et al. 2004), but in the rest-frame UV part of their spectra. In the UV these galaxies appear compact ($r \sim 0.''2 - 0.''3$, ~ 1.5–$3\ h^{-1}$ kpc), in good qualitative agreement with the predictions for the buildup of stellar mass from hierarchical formation scenarios (Mo, Mao, & White 1999). However, the selection technique and the observed rest-frame wavelength raise the following question: are the galaxies selected (LBGs) and the sizes measured (UV sizes) representative of the radial stellar mass distribution of the luminous high-z galaxy population? Put differently, is the radial extent of the instantaneous, relatively unobscured star formation, which is measured by the rest-frame far-UV light, indicative of the radial extent of the stellar mass distribution?

To properly test the model predictions, one would ideally like to trace the size evolution of galaxies in the optical (rather than UV) rest frame at every redshift. Any observed size evolution would then reflect true evolutionary changes not subject to the changing appearance of galaxies in different bandpasses, an effect known as the morphological k-correction. Most of the past studies using constant rest-frame bands have been limited to modest redshifts ($z \lesssim 1$; e.g., Lilly et al. 1998) as a result of the dearth of very deep near-infrared (NIR) images that allow one to reach the rest-frame optical.

To map the size evolution of the stellar body of galaxies, it is necessary to conduct an analysis at wavelengths at least as red as the rest-frame optical. At $z \gtrsim 0.8$ this implies selecting and analyzing galaxies from very deep NIR images. In this paper we use data for the Hubble Deep Field–South (HDF-S) from the Faint Infrared Extragalactic Survey (FIRES; Franx et al. 2000) to address this issue.[7] We use these data to

[1] Based on observations collected at the European Southern Observatory, Paranal, Chile (ESO LP 164.O-0612), and also on observations with the NASA/ESA *Hubble Space Telescope*, obtained at the Space Telescope Science Institute, which is operated by AURA, Inc., under NASA contract NAS 5-26555.

[2] Max-Planck-Institut für Astronomie, Königstuhl 17, 69117 Heidelberg, Germany.

[3] Max-Planck-Institut für Astrophysik, Postfach 1317, D85748 Garching, Germany.

[4] Leiden Observatory, University of Leiden, P.O. Box 9513, Leiden NL-2300 RA, Netherlands.

[5] European Southern Observatory, D-85748 Garching, Germany.

[6] Department of Astronomy, Yale University, P.O. Box 208101, New Haven, CT 06520-8101.

[7] The size properties of galaxies in the MS 1054−03 FIRES field (N. M. Förster Schreiber et al. 2004, in preparation) will be discussed in a forthcoming paper.

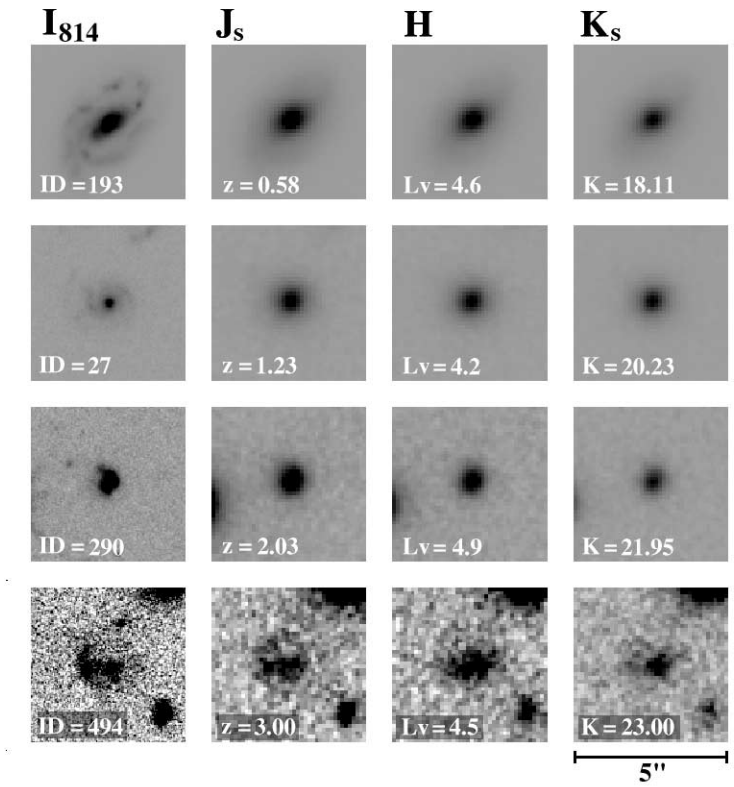

FIG. 1.—Mosaic of similar rest-frame *V*-band luminosity galaxies at different redshifts. The apparent *K*-band magnitude decreases toward the bottom. The luminosities are given in $10^{10}\ L_{\odot}$. The galaxies are shown in four different filters.

constrain the size evolution; i.e., we test whether for a given rest-frame luminosity, or a given stellar mass, the sizes of the high-*z* population are equal to or different from those of nearby galaxies. To assess the degree of evolution, if any, it is crucially important that good local calibrating data be available. With the advent of large local surveys (e.g., the Sloan Digital Sky Survey [SDSS]; York et al. 2000), we now have complete samples of local galaxies with accurate measurements of fundamental properties such as luminosity or size to use as low-redshift reference points.

This paper is organized as follows: The data and the measurement technique are described in § 2. In § 3 we present the luminosity-size and mass-size relations of the high-*z* galaxies and discuss how selection effects play a role in interpreting the observed trends. In § 4 we describe a simulation of how the local galaxy population (as provided by the SDSS data) would appear at high *z*. By comparing with the FIRES data, we constrain the size evolution for the galaxies in our sample. Finally, in § 5 we discuss our results.

2. OBSERVATIONS, DATA, AND SIZE DETERMINATIONS

2.1. *Data and Catalog Construction*

Ultradeep NIR images of the HDF-S were obtained as part of FIRES, and the data processing and photometry are discussed in detail by Labbé et al. (2003a).[8] Briefly, using ISAAC (Moorwood 1997; field of view of $2\farcm5 \times 2\farcm5$ and pixel scale $0\farcs119$)[9] on the VLT, the HDF-S was imaged for 33.6 hr in J_s, 32.3 hr in *H*, and 35.6 hr in K_s. The effective seeing in the reduced images is approximately $0\farcs47$ in all bands. The depth ($3\ \sigma$) reached was 26.8 mag in J_s, 26.2 mag in *H*, and 26.2 mag in K_s for point sources. All magnitudes in this paper are given in the AB system unless stated explicitly otherwise. Some examples of galaxies in these ultradeep images are presented in Figure 1. Combining these NIR data with deep optical *HST* WFPC2 imaging (ver. 2; Casertano et al. 2000), we assembled a K_s-selected catalog containing 833 sources, of which 624 have seven-band photometry, covering 0.3–2.2 μm. Stars were identified and removed from the catalog if their spectral energy distributions (SEDs) were better fitted by a single stellar template than by a linear combination of galaxy templates. Four of the stellar candidates from this color classification were obviously extended and were reidentified as galaxies. Two bright stars were not identified by their colors because they are saturated in the *HST* images and were added to the list by hand. Photometric redshifts were estimated for the cataloged galaxies following Rudnick et al. (2001; see also § 3).

The sample of galaxies is selected in the K_s band. For $z \lesssim 3$ this filter reflects galaxy flux at wavelengths redder than the rest-frame *V* band and so selects galaxies in a way that is less sensitive to their current unobscured star formation rate than selection in the rest-frame UV. To select galaxies with reliable photometry, we exclude the much less exposed borders of our combined K_s "dithered" image (see Labbé et al. 2003a), taking only those galaxies whose fractional exposure time is

[8] The catalog and reduced images are available at http://www.strw.leidenuniv.nl/~fires.

[9] The ISAAC pixel scale is actually $0\farcs147$; however, we resampled the ISAAC pixels to 3×3 blocked HDF-S WFPC2 pixels.

$\geq$35% of the maximum. To ensure sufficient signal-to-noise ratio for the subsequent size determinations, we limit ourselves to the 171 objects with $K_s \leq 23.5$ and with ISAAC and WFPC2 coverage.

2.2. *Measuring Sizes*

The multiband imaging allows us to make a homogeneous comparison of the rest-frame optical size for all sample galaxies at redshift $z \lesssim 3$. We measure the sizes of galaxies at all redshifts consistently by fitting the profile of each galaxy in the bandpass that corresponds most closely to the rest-frame V band at that redshift: for $0 < z < 0.8$ we fit the I_{814} band, for $0.8 < z < 1.5$ the J_s band, for $1.5 < z < 2.6$ the H band, and for $2.6 < z < 3.2$ the K_s band.

At high redshift the angular sizes of typical galaxies in our sample are comparable to the size of the seeing ($\sim$0.″47). Consequently, the intrinsic structure and size of the galaxies must be obtained by adopting a surface brightness (SB) model and convolving it with the image point-spread function (PSF). This approach is well tested and successful at fitting low-z galaxies.

We seek a flexible parametric description of the galaxies' SB distribution, without resorting to multicomponent models. The population of galaxies at any redshift is likely a mixture of spiral galaxies, elliptical galaxies, and irregular objects. Elliptical galaxies (from dwarfs to cDs) are well fitted by a Sérsic model $r^{1/n}$ (Sérsic 1968), as demonstrated by a number of authors (see, e.g., Trujillo, Graham, & Caon 2001b and references therein). The Sérsic model is given by

$$I(r) = I(0) \exp\left[-b_n \left(\frac{r}{r_e}\right)^{1/n}\right], \quad (1)$$

where $I(0)$ is the central intensity and r_e the effective radius, enclosing half of the flux from the model light profile. The quantity b_n is a function of the radial shape parameter n, which defines the global curvature in the luminosity profile, and is obtained by solving the expression $\Gamma(2n) = 2\gamma(2n, b_n)$, where $\Gamma(a)$ and $\gamma(a, x)$ are, respectively, the gamma function and the incomplete gamma function.

The disks of spiral galaxies are also well described by a Sérsic model with $n = 1$, corresponding to an exponential profile. The Sérsic model (with its free shape parameter n) is flexible enough to fit the radial profiles of nearly every galaxy type.[10] For this reason and for its simplicity, we decided to use it for measuring the sizes of galaxies in our data.

Both the intrinsic ellipticities of the galaxies and the effects of the seeing on the images were taken into account when fitting the model. Details of the particular model fitting method are given in Trujillo et al. (2001a) and Aguerri & Trujillo (2002).

We start by measuring the SB and ellipticity profiles along the major radial axis by fitting isophotal ellipses to the sample object images, using the task ELLIPSE within IRAF.[11] The fits extend down to 1.5 times the standard deviation of the sky background of the images. Some examples of the model fits to our sample galaxies are presented in Figure 2. A Levenberg-Marquardt nonlinear fitting algorithm (Press et al. 1992) was used to determine the set of free parameters that minimizes χ^2. To do this, we fit simultaneously the observed one-dimensional and ellipticity profiles using a PSF-convolved model for each. In what follows, we refer to the "circularized effective radius" of the fitted model, i.e., $r_e = a_e(1-\epsilon)^{1/2}$, as the *size* of the galaxies; here a_e is the semimajor effective radius and ϵ the projected ellipticity of the galaxy model. We checked that the estimate of the intrinsic ellipticity of our sources, and hence the conversion to circularized effective radius, was not systematically affected by the seeing, by searching for trends with z or the K_s apparent magnitude (Fig. 3). No significant trends were found.

The PSF was estimated for every band by fitting a Moffat function to star profiles. We find the following β and FWHM as our best-fitting stellar parameters: $\beta = 2.5$, FWHM = 0.″147 (I_{814} band); $\beta = 3$, FWHM = 0.″46 (J_s band); $\beta = 3$, FWHM = 0.″49 (H band); and $\beta = 3$, FWHM = 0.″47 (K_s band). When fitting objects close to the resolution limit, it is crucial to have an accurate measure of the PSF. To test the robustness of our size measurements against slight errors in our PSF determination, we compared our sizes to those determined using a completely independent fitting algorithm (GALFIT; Peng et al. 2002). This code uses the two-dimensional profiles of the stars themselves to convolve the models with the seeing. In Figure 4 we show the relative error between the size estimates using both our code and GALFIT. The difference between the sizes does not show any clear trend with z or the apparent K_s magnitude. The agreement between these two different algorithms ($\sim$68% of the galaxies have a size difference less than 35%) corroborates the robustness of the size determination. One reason for this is that our very deep NIR data allow us to sample the profiles out to approximately 2 effective radii, providing ample constraints for the fit. For the smallest objects, our bright total magnitude limit ($K_s = 23.5$) has the effect that the measured SB profile extends over 5 mag and is therefore very well characterized. The size errors of each galaxy are taken into account in the subsequent analysis.

There are three galaxies where the size estimation is ill defined because they have a close companion. These galaxies represent only $\sim$1.5% of the total and are all at $z < 1.15$. The final sample is composed of 168 galaxies. The sizes of these galaxies are shown in Table 1.

One way to test the quality of our model fits is to compare the model magnitude with an aperture isophotal magnitude (Labbé et al. 2003a; see Fig. 5). The total luminosity, L_T, associated with an $r^{1/n}$ profile extended to infinity can be written as

$$L_T = I(0) r_e^2 \frac{2\pi n}{b_n^{2n}} \Gamma(2n). \quad (2)$$

As expected for an extrapolation to infinity, the total model magnitude is almost always equal or brighter than the model-independent determination. In general, there is relatively good agreement between the two measures: a magnitude difference less than 0.2 mag for 75% of the sample. The difference between the two estimators is largest for objects with the highest n-values, as expected because of the large amounts of light at large radii in these models (Trujillo et al. 2001b). Galaxies, however, certainly do not extend to infinity, and the model

[10] Even early-type spirals composed by a bulge plus a disk can be fitted by a single Sérsic model (Saglia et al. 1997).

[11] IRAF is distributed by the National Optical Astronomical Observatory, which is operated by AURA, Inc., under contract to the NSF.

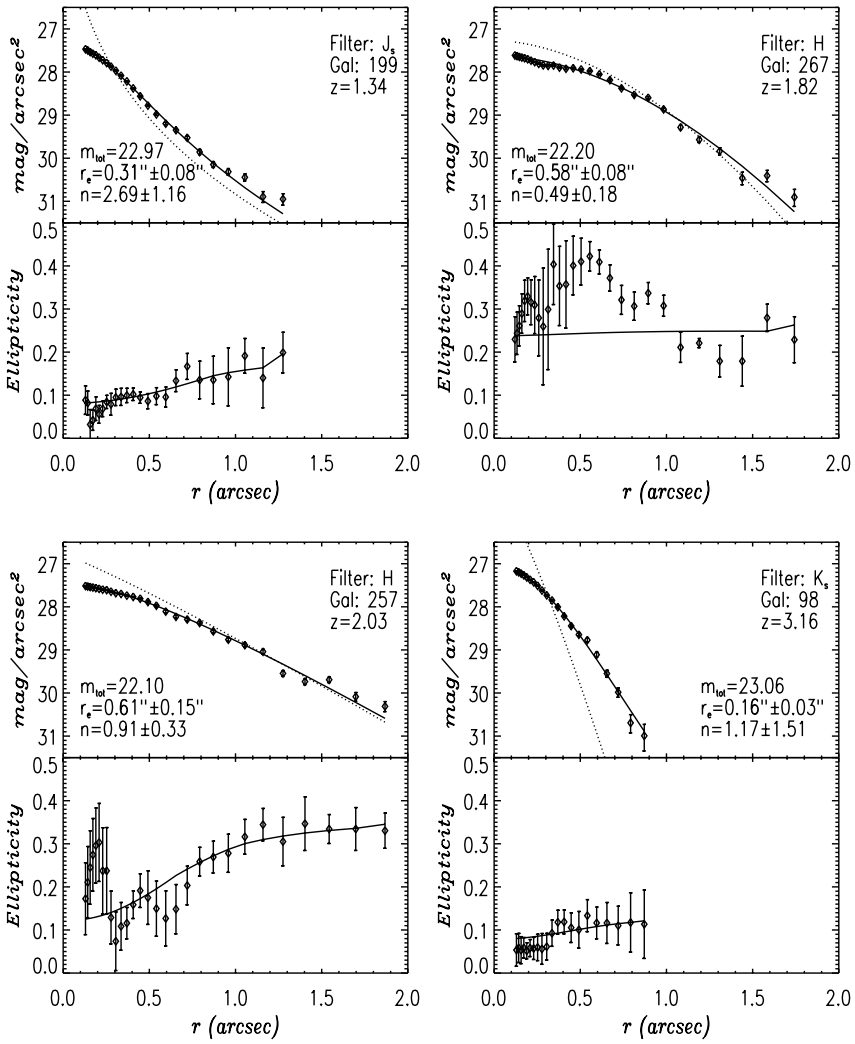

FIG. 2.—SB and ellipticity semimajor radial profiles fitting to four galaxies in our sample. Every galaxy is fitted in its optical rest-frame band following the criteria explained in the text. The galaxy identification numbers correspond to the catalog identification (see Labbé et al. 2003a). Superimposed on the SB profile data are the model profile (*dashed line*) and the convolution of this model profile (*solid line*) to match the data. The solid lines in the ellipticity radial profiles show the fit to the ellipticities using our algorithm. Intrinsic ellipticities (i.e., not seeing convolved) of the galaxies can be obtained by extrapolating to infinity the solid lines. Details of the fitting algorithm can be found in Trujillo et al. (2001a) and Aguerri & Trujillo (2002).

extrapolation is likely unphysical, especially for high-n values. For this reason we choose the total luminosity from Labbé et al. (2003a) in the following analysis.

3. THE OBSERVED LUMINOSITY/MASS VERSUS SIZE RELATIONS AT HIGH z

We now present the relations between stellar luminosity, or stellar mass, and the rest-frame V-band size over a wide range of redshift. Throughout we assume $\Omega_M = 0.3$, $\Omega_\Lambda = 0.7$, and $H_0 = 100\,h$ km s^{-1} Mpc^{-1}. We convert our measured angular sizes to physical sizes using the photometric redshift determined for each object.[12] These redshifts, as well as the rest-frame optical luminosities, were estimated by fitting a linear combination of nearby galaxy SEDs and model spectra to the observed flux points (Rudnick et al. 2001, 2003). The accuracy derived from 39 available spectroscopic redshifts is very good, with $|z_{\rm phot} - z_{\rm spec}|/(1+z_{\rm spec}) \approx 0.05$ for $z > 1.4$. A plot of the $z_{\rm spec}$ versus $z_{\rm phot}$ for the present sample is shown in Labbé et al. (2003a; see their Fig. 6). We neglect the photometric redshift uncertainties in our analysis since a redshift error of even ± 0.5 at $z = 1.5$ corresponds to size errors of $\lesssim$5%. On the other hand, our photometric redshift uncertainties equate to $\lesssim$35% luminosity errors. For a first analysis step, we have split our sample into a $z \leq 1.5$ and a $z > 1.5$ bin and plot the rest-frame optical effective radius (the size estimated in the rest-frame band filter) versus the total luminosity in the rest-frame V band in Figure 6.

We also have explored the relation between stellar mass and size for our sample (see Fig. 6). The stellar mass-to-light ratios (M/L) and hence stellar masses for the individual galaxies were estimated by G. Rudnick et al. (2004, in preparation) from their rest-frame colors and SEDs, using a technique similar to that of Bell & de Jong (2001). Briefly, this approach exploits the relation between color and M/L, which exists over a wide range of monotonic star formation histories and is rather robust against the effects of age, dust extinction, or metallicity. Errors in the derived masses will occur in the presence of bursts. In practice, we derive the M/L from the rest-frame $(B-V)$ color using the models presented in Bell & de Jong (2001). We take into

[12] For 25% of the galaxies in our sample z was determined spectroscopically. When a $z_{\rm spec}$ determination is available, this is the value used.

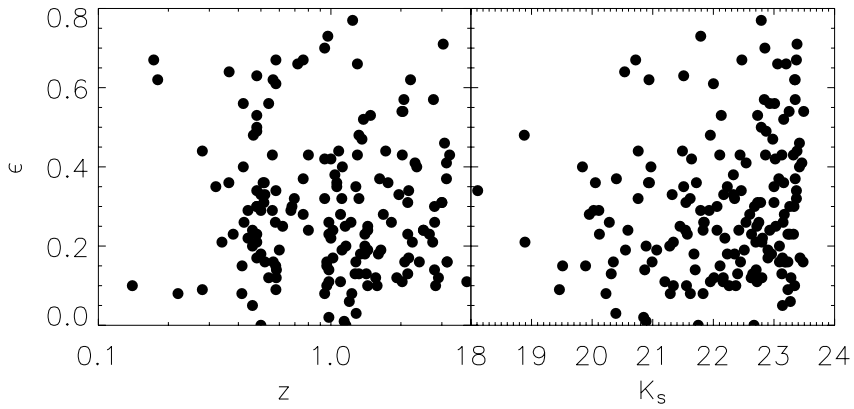

FIG. 3.—Intrinsic (i.e., the recovered nonseeing affected) ellipticity of the galaxies vs. the redshift of the observed sources (*left*) and the apparent K_s total magnitudes (*right*). No clear relation is observed.

account the photometric redshift probability distribution and the scatter in the $(B-V)$–M/L relation when calculating our uncertainties (G. Rudnick et al. 2004, in preparation).

3.1. *Selection Effects*

For studying galaxy size evolution from Figure 6, we must understand the selection effects at play in our sample. Redshift-dependent observational biases can mimic real evolutionary changes in the galaxy population, both through biases in the selection of galaxies and through the measurement of their sizes. Knowing the selection effects is also crucial in creating mock high-redshift catalogs from low-redshift surveys.

For a given flux limit (in our case $K_s = 23.5$) there is a corresponding threshold in the rest-frame luminosity, which increases with redshift. This is well illustrated in the L_V-z diagram (Fig. 7) and demonstrates that our high-z sample represents only the most luminous fraction of the galaxy population. The absence of bright galaxies at low redshift is largely due to the small volume of the HDF-S over this redshift range.

The detectability of an object, however, depends not only on its apparent magnitude but also on its morphology and mean SB: for a given apparent magnitude, very extended, and hence low-SB, objects will have a lower signal-to-noise ratio than a compact source. In practice, any image presents an SB limit beyond which the sample will be incomplete. For a given flux limit, the SB limit translates, therefore, into an upper limit on the size for which an object can still be detected. To determine the completeness of the FIRES K-band image, we created 100,000 artificial galaxies with intrinsic exponential profiles and with structural parameter values covering the ranges $18 < K_s < 24$, $0\farcs03 < r_e < 3\farcs0$, and $0^\circ < i < 90^\circ$.[13] The model images were randomly placed, 20 at a time, into

[13] Galaxies with values of n bigger than 1 are more centrally concentrated than an exponential and, hence, are easier to detect at a given total magnitude. Therefore, our choice of $n = 1$ is a conservative one. We do note, however, that objects with $n < 1$ will be harder to detect at a given total magnitude; such objects are found to be dwarf (faint) galaxies in the local universe, and we assume that they will not be observed in our high-z sample.

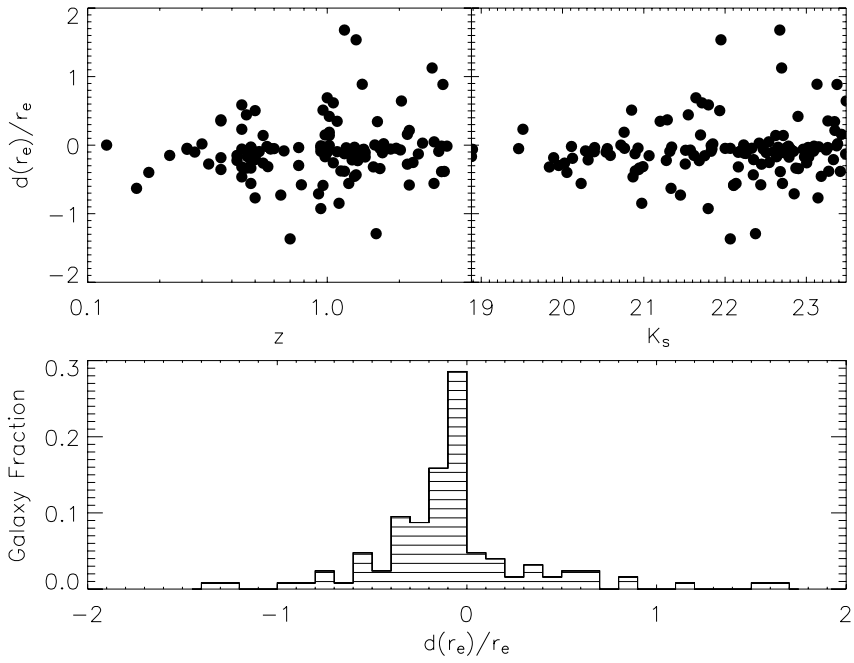

FIG. 4.—Relative error between the size estimation using our code and GALFIT $d(r_e)/r_e = 2[r_e(\mathrm{GALFIT}) - r_e(\mathrm{ours})]/[r_e(\mathrm{GALFIT}) + r_e(\mathrm{ours})]$ shown vs. z and vs. the apparent K_s magnitude. No clear trend is found. The histogram shows that for ~68% of the galaxies the difference is less than 35%.

TABLE 1
PROPERTIES OF THE SAMPLE GALAXIES

Galaxy (1)	X (2)	Y (3)	$K_{s,\mathrm{tot}}$ (4)	r_e (arcsec) (5)	ϵ (6)	L_V ($10^{10}\ h^{-2}\ L_\odot$) (7)	M_* ($10^{10}\ h^{-2}\ M_\odot$) (8)	z (9)	Filter (10)
793.....	3538.3	3496.9	21.33	0.04	0.10	0.01	0.01	0.140	I_{814}
244.....	2272.6	1587.5	20.71	0.40	0.67	0.06	0.09	0.173*	I_{814}
283.....	2063.5	1660.1	23.34	0.51	0.62	0.01	0.01	0.180	I_{814}
314.....	2741.5	1815.3	21.61	0.24	0.08	0.02	0.02	0.220	I_{814}
288.....	501.6	1633.9	23.23	0.39	0.09	0.01	0.02	0.280	I_{814}
464.....	943.0	2017.5	20.76	0.30	0.44	0.11	0.20	0.280	I_{814}
227.....	1393.0	1430.0	21.51	0.60	0.35	0.12	0.17	0.320	I_{814}
184.....	626.9	1387.0	18.89	0.55	0.21	0.75	1.92	0.340*	I_{814}
446.....	2417.6	2080.2	20.05	0.56	0.36	0.39	1.11	0.364*	I_{814}
528.....	2478.4	3018.5	20.53	0.71	0.64	0.28	0.42	0.365*	I_{814}

NOTES.—Col. (1): Catalog identification numbers (see Labbé et al. 2003a). Cols. (2) and (3): X and Y pixel coordinate positions in the HDF-S mosaic. Col. (4): K_s-band total magnitudes. Col. (5): Circularized rest-frame half-light radii. The typical uncertainty on the size determination is 35%. Col. (6): Intrinsic (i.e., the recovered nonseeing affected) ellipticity. Col. (7): Rest-frame V-band luminosity. The typical uncertainty on the luminosity determination is 30%. Col. (8): Stellar mass. Col. (9): Redshift (asterisk means spectroscopic z). Col. (10): Filter used to measure the size of the galaxies. Table 1 is published in its entirety in the electronic edition of the *Astrophysical Journal*. A portion is shown here for guidance regarding its form and content.

the K_s-band image, and SExtractor was run using the same parameters that were used to detect the real galaxies. Figure 8 shows the fraction of galaxies successfully detected by SExtractor at each input value (K_s, r_e). Superimposed in Figure 8, we show the K_s-band size and apparent magnitude for our sample objects. Also shown are lines of constant central SB for exponential models ($n = 1$). Even for the conservative assumption of an exponential profile, we are complete over almost the entire range spanned by our sample galaxies. This can be understood simply because our NIR images are so deep. Our sample selection threshold is $\sim$3 mag brighter than the 3 σ detection limit.

The exact SB limit for real distributions of galaxies is more complex, as galaxies have a range of profile shapes, with different Sérsic indices n and hence different central SBs. Indeed, the data show no clearly defined threshold. Nonetheless, as a conservative estimate of our completeness limit we adopt a threshold at a central SB of $\mu_K(0) = 23.5$ mag arcsec^{-2}, for which we are 90% complete for an exponential model. Objects with this $\mu_K(0)$ that are more concentrated than an exponential would be detected with even more completeness than 90%. We have also found that, at the SB limit, we can retrieve the sizes to within $\sim$20% of objects with $n = 1$. However, for exponential objects near our SB limit, we underestimate the magnitude by a median of 0.25 mag (and greater than 0.4 mag for 25% of these objects). This has to do with the way SExtractor measures magnitudes, which depends on apparent SB. We have also checked for possible incompleteness effects around the observed $K_s = 23.5$ magnitude limit because of small systematic underestimates of measured magnitudes, but we find that they are not significant. The corrections to total magnitudes for observed galaxies near the SB limit are, however, uncertain. To be conservative, we choose not to correct the flux at the SB limit and note that the application of any correction for missed flux would simply increase the derived luminosities of our galaxies.

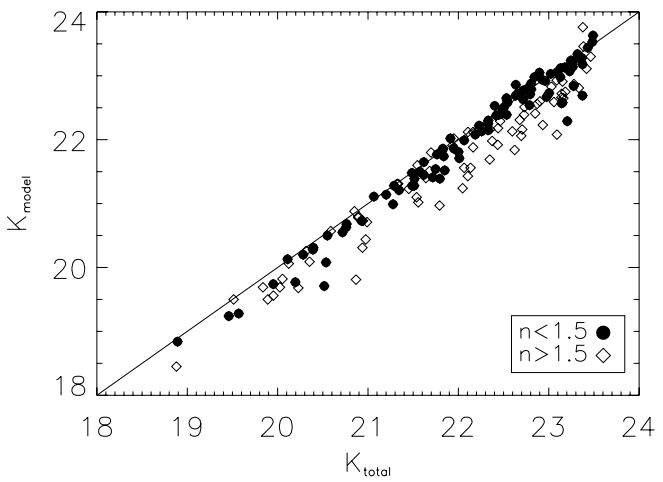

FIG. 5.—Total magnitude retrieved from the model fitting compared to the total magnitude measured in a model-independent way for the galaxies analyzed in this paper. Galaxies with $n < 1.5$ are shown by filled circles and galaxies with $n > 1.5$ by open diamonds.

In Figure 9 we show how our conservative SB limit translates into the 90% completeness track in the parameter plane of r_e and $L_{V,\mathrm{rest}}$. For a given redshift, we are less than 90% complete for exponential galaxies with an effective radius larger than the corresponding line in Figure 9. Because of $(1+z)^4$ SB dimming, redshift plays a very large role in this detectability. Similarly, for a given luminosity the maximal disk size to which we are complete will decrease with increasing redshift.

4. ANALYSIS

The selection effects will affect the distribution of points in Figure 6 and make it impossible to read off any size evolution, or lack thereof, without careful modeling. We explore evolutionary trends in the distribution of the galaxies in the above diagrams, by taking a $z = 0$ luminosity-size (and mass-size) relation and by drawing mock high-redshift catalogs from these relations, subject to the redshift-dependent selection effects.

4.1. *Simulating the Local Luminosity/Mass versus Size Relations at High Redshifts*

The SDSS (York et al. 2000) is providing an unprecedented database of $\sim 10^6$ nearby galaxies with spectroscopic redshifts

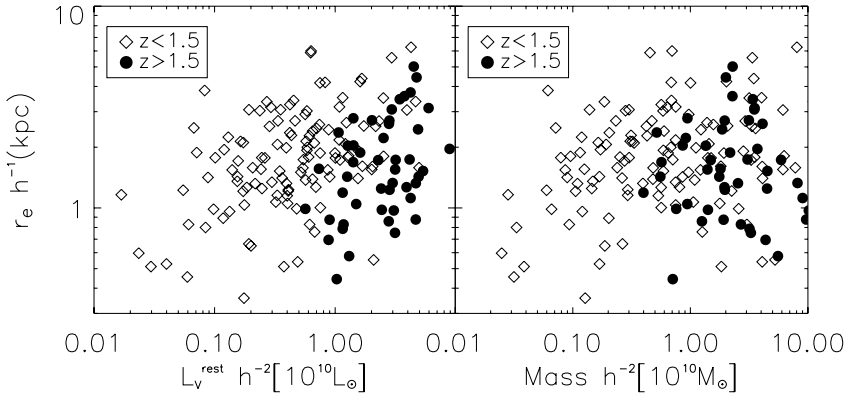

FIG. 6.—*Left*: Distribution of rest-frame optical sizes vs. the rest-frame *V*-band luminosities. Galaxies with redshifts smaller than 1.5 are shown by open diamonds and galaxies with redshifts bigger than 1.5 by filled circles. *Right*: Same as in the left panel, but with the stellar mass. For clarity error bars are not shown. The mean size relative error is 35%.

and multiband photometry. In particular, it has been used to derive the size distribution of present-epoch galaxies versus their luminosities and stellar masses (Shen et al. 2003). Shen et al. (2003) show the median and dispersion of the distribution of Sérsic half-light radius (Blanton et al. 2003) for different bands as a function of the luminosity and of the stellar mass. We have used their *g*-band (the closest available filter to our *V* band) size distributions (S. Shen 2003, private communication) as a local reference of the size distribution of galaxies in the nearby universe. We note that whereas Shen et al. (2003) show separately the distribution of early- and late-type galaxies, we use their combination of these two subsamples into one, to make a direct comparison with our sample. For nearby galaxies of a given luminosity, Shen et al. (2003) propose the following size lognormal distribution with median $\bar{r}_e$ and logarithmic dispersion σ:

$$f(r_e|\bar{r}_e(L),\sigma(L)) = \frac{1}{\sqrt{2\pi}\sigma(L)}\exp\left\{-\frac{\ln^2[r_e/\bar{r}_e(L)]}{2\sigma^2(L)}\right\}\frac{dr_e}{r_e}, \quad (3)$$

illustrated in Figure 10.

The SDSS relations are used to test the null hypothesis, i.e., that the luminosity-size or mass-size relations do not change with redshift. It is important to note that this does not imply

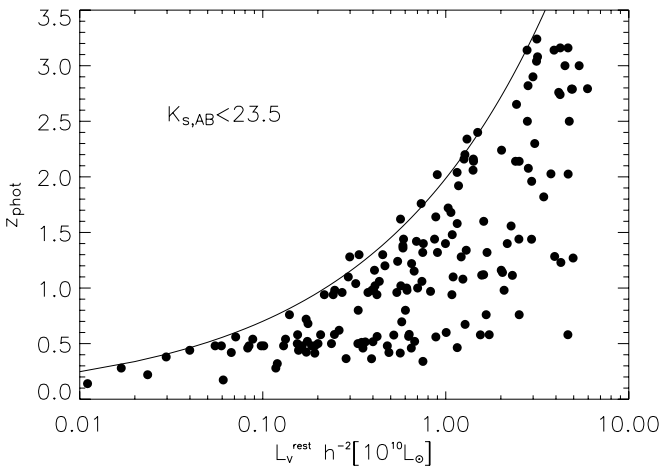

FIG. 7.—The L_V-z diagram for the objects selected in our sample with $K_s < 23.5$. The tracks represent the values of $L_V^{\rm rest}$ for Scd template spectra (see Fig. 11*c* in Rudnick et al. 2001) normalized at each redshift to $K_{s,\rm AB} = 23.5$.

that the galaxies themselves do not change; they could certainly evolve "along" such a relation. To test the null hypothesis, we construct distributions of SDSS galaxies as they would be observed at high redshift, mimicking our observations as follows: Every simulated distribution of galaxies contains the same number of objects as our FIRES sample (i.e., 168). We pick a luminosity and redshift pairs at random from our observed sample. For this luminosity L, we evaluate a size at random from the local size sample distribution provided by the SDSS data (eq. [3]), by solving the following implicit equation:

$$F(r_e|L) = \frac{1}{2}\left(1 - \Phi\left\{\frac{\ln[r_e/\bar{r}_e(L)]}{\sqrt{2}\sigma(L)}\right\}\right), \quad (4)$$

where Φ is the error function and $F(r_e|L)$ is randomly distributed in [0, 1].

For every effective radius drawn from equation (4) we analyze if this galaxy (characterized by r_e, L, z) would be observed within the completeness limit of Figure 9. If it is larger, it is not taken into account in our simulated distribution. The process for selecting a new galaxy is repeated until we have a mock sample with the same number of objects as galaxies observed.

This procedures assures that the simulated galaxy distribution follows the same redshift and luminosity distribution as the observed sample and also is affected by the same selection effects. An analogous procedure is repeated in the case of the size-mass relation replacing L with M_* in equations (3) and (4).[14] At this time, to account for the selection effects, we select an (M/L, L, z) triplet at random from the observed distribution.

Figure 11 shows an example of how the SDSS galaxies would be distributed in the size diagrams with the same luminosity, mass, and redshift distribution as the galaxies observed in FIRES. A comparison of Figures 6 and 11 shows that the simulated SDSS data have luminosity-size and mass-size relations that are tighter than the observed FIRES relations. If the luminosity-size relation from SDSS remained unchanged with increasing z, we would not expect to find

[14] Shen et al. (2003) use also a lognormal distribution for the size-mass relation. Their mass evaluation rests in the Kroupa (2001) initial mass function (IMF). The stellar mass modeling of the FIRES data, however, uses a Salpeter IMF. In our simulations we have followed the procedures suggested in Kauffmann et al. (2003) of using $M_{\rm IMF,Salpeter} = 2M_{\rm IMF,Kroupa}$ to transform from SDSS data to our data.

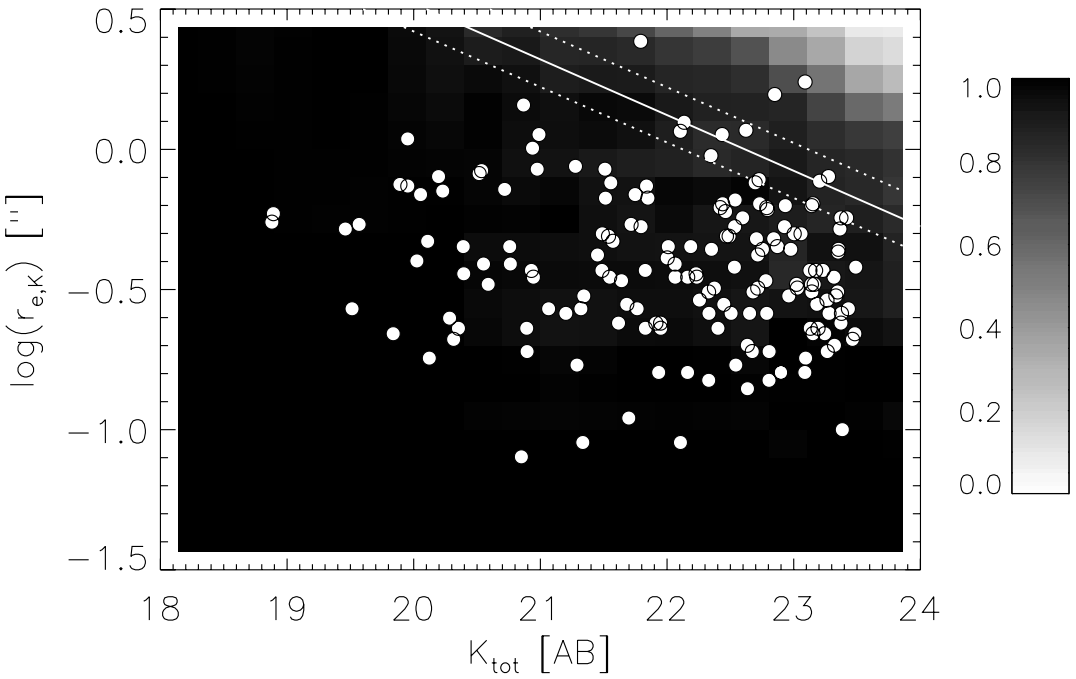

FIG. 8.—Completeness map for detecting galaxies with exponential profiles in the FIRES *K*-band data. The horizontal and vertical axes represent the input values. Overplotted is the K_s-band size vs. the apparent K_s magnitude for the objects in our sample (*white circles*). We have also shown exponential models ($n = 1$) with central SB of 23 and 24 mag arcsec^{-2} (*dotted lines*). The solid line represents the central surface brightness [$\mu_K(0) = 23.5$ mag arcsec^{-2}] at which we are 90% complete.

small and luminous objects at high redshift; however, these objects are present in the FIRES observations (see Fig. 6).

To quantify if these qualitative differences between the observed distributions and the simulated null hypothesis are significant, we ran the generalization of the Kolmogorov-Smirnov (K-S) test to two-dimensional distributions (Fasano & Franceschini 1987). We create 1000 SDSS realizations (for both luminosity and mass). For all the simulations the rejection probability is bigger than 99.9%. Consequently, we conclude that neither the luminosity-size nor the mass-size observed relation satisfies the null hypothesis.

To account for measurement errors in the size estimates of the FIRES galaxies, we also create mock "FIRES" data point distributions. To create these distributions, we randomly vary every observed effective radius using a normal distribution with standard deviation equal to the size error measured for each galaxy. We make 1000 mock "FIRES" distributions and compare for each the rejection probability between the SDSS and the mock "FIRES" data. The rejection probability for all mock samples is again more than 99.9% in the luminosity and the mass relations. Thus, the intrinsic dispersion of our measurements is unable to explain the difference with the SDSS simulated data.

We also explored the sensibility of the adopted FIRES selection limits through simulations: we have evaluated the SDSS distribution function including different central SB limit ranging from 23 to no restrictions at all. We do not find any significant difference in our results. As we expected because of the depth of our images, uncertainties in the selection effects do not affect our analysis.

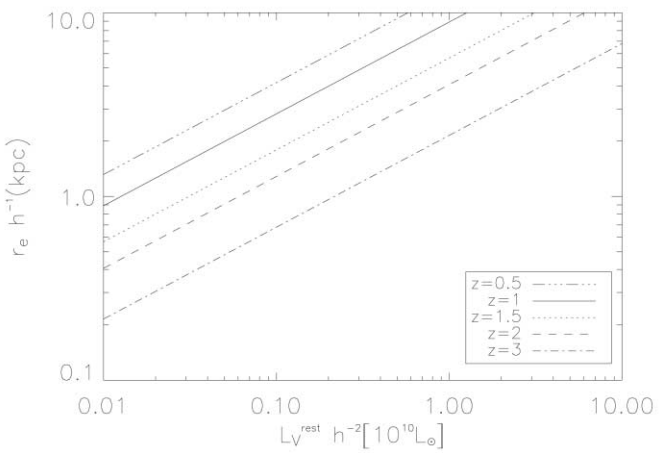

FIG. 9.—The 90% completeness tracks in effective radius for an exponential model with central SB at K_s of 23.5 mag arcsec^{-2} (see Fig. 8). We adopt these conservative limits when creating mock high-redshift catalogs of SDSS galaxies. To convert from observed *K*-band magnitudes to rest-frame *V*-band luminosities, we used an Scd template (see Fig. 11*c* in Rudnick et al. 2001).

4.2. *Testing the Hypothesis of Evolution*

The no-evolution hypothesis, that the size relations for all galaxies are redshift independent, can be rejected for both the L_V-r_e and M_*-r_e relations. To quantify and constrain the evolution of these relations with redshift, we need to devise an evolution model. In the absence of clear-cut theoretical predictions, we have resorted to a heuristic parameterization that draws on the observed local distribution. We have assumed that the lognormal size distribution (eq. [3]) applies at all redshifts, but with evolving parameters:

$$\bar{r}_e(L, z) = \bar{r}_e(L,\ 0)(1 + z)^{-\alpha}, \tag{5}$$

$$\sigma(L, z) = \sigma(L,\ 0)(1 + z)^{\beta}. \tag{6}$$

Here $\bar{r}_e(L,\ 0)$ and $\sigma(L,\ 0)$ are the median size and dispersion provided at $z = 0$ by the Shen et al. (2003) data, and α and β describe the redshift evolution. Note that equations (5) and (6)

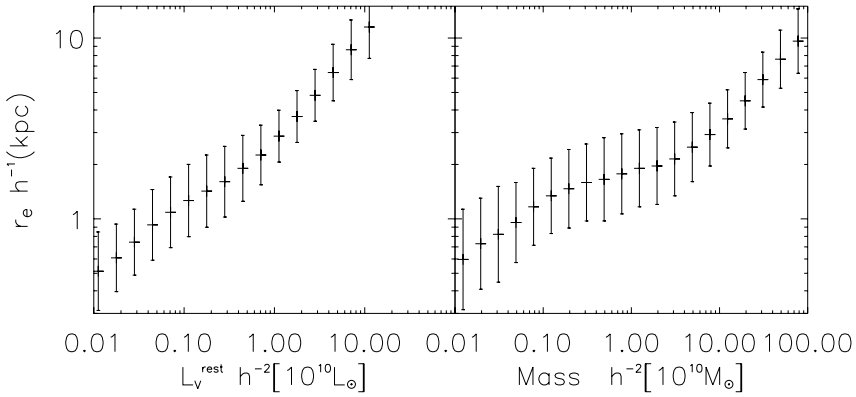

FIG. 10.—*Left*: Median and dispersion of the distribution of the Sérsic half-light radius of the SDSS galaxies (in the *g* band) as a function of the *g*-band luminosity (the closest available filter to our *V* band). *Right*: Same as in the left panel, but as a function of the stellar mass. Note that the luminosity (mass) extends in this figure up to 10^{12} solar luminosities (masses).

imply the same size evolution for all the galaxies independently of their luminosity. We also assume an analogous parameterization for the masses. For both L_V-r_e and M_*-r_e we explore the ranges $[-2, 3]$ for α and $[-2, 2]$ for β.

As for the null hypothesis, we generate simulated galaxy distributions for every pair (α, β) and we ran a K-S test between these simulations and the observed data. Neither for L_V-r_e nor for M_*-r_e could we produce evolutionary scenarios (α, β) whose distribution functions are in agreement with what we see in the FIRES data. However, one must bear in mind that not all the luminosities can be observed over the full redshift range (see Fig. 7). To understand better what possible evolution our data imply and to avoid luminosity-dependent redshift ranges, we decided to create more homogeneous subsamples by splitting our sample into three different luminosity (mass) bins. Both our luminosity-size and mass-size observed distributions have been divided in three luminosity (mass) bins as detailed in Table 2.[15] The splitting of our sample into these intervals avoids that low-luminosity (mass) galaxies at low redshift dominate the results of our analysis. The mean redshifts for the low-, intermediate-, and high-luminosity (mass) bins are 1.0, 1.6, and 2.0, respectively. These different sets measure evolution in a different luminosity (mass) range and a different redshift range, and splitting them helps to make this clear.

We now can check whether the observed FIRES relations can be explained if the evolutionary parameters α and β depend on the luminosity (mass) and write out the new distribution function explicitly, combining equations (5) and (6) with equation (3):

$$g(r_e|\bar{r}_e, \sigma, z) = \frac{1}{\sqrt{2\pi}\sigma}\frac{dr_e}{r_e}\frac{dz}{(1+z)^\beta} \times \exp\left\{-\frac{\ln^2[r_e/\bar{r}_e(1+z)^\alpha]}{2\sigma^2(1+z)^{2\beta}}\right\}. \quad (7)$$

The expression in equation (7) is a probability density, and we use this to evaluate α and β using a maximum likelihood method. For each luminosity/mass subsample we show in Figure 12 the likelihood contours (1 and 2 σ) in the plane of α and β. We have also included as a reference the point $\alpha = 0$ and $\beta = 0$, which indicates the case of no evolution at this plane. The top panels show the evolution of the size distribution at a given luminosity. The mean size at a given luminosity changes significantly for luminous galaxies: at $\langle L_V \rangle \sim 2 \times 10^{10}\, h^{-2}\, L_\odot$ galaxies were typically 3 times smaller at $z \sim 2.5$ than now and 4 times smaller for $L_V > 3 \times 10^{10}\, h^{-2}\, L_\odot$. A luminosity-independent model (α and β independent of L) is less likely than our luminosity-dependent model, justifying our choice of

[15] The lowest luminosity (mass) galaxies with $L < 0.3 \times 10^{10}\ L_\odot$ ($M_* < 0.3 \times 10^{10}\ M_\odot$) are not presented in this analysis. These galaxies have $z \lesssim 1$ and, consequently, the results coming from this subsample are largely affected by the cosmic variance associated with the small volume enclosed in the HDF-S over this redshift range.

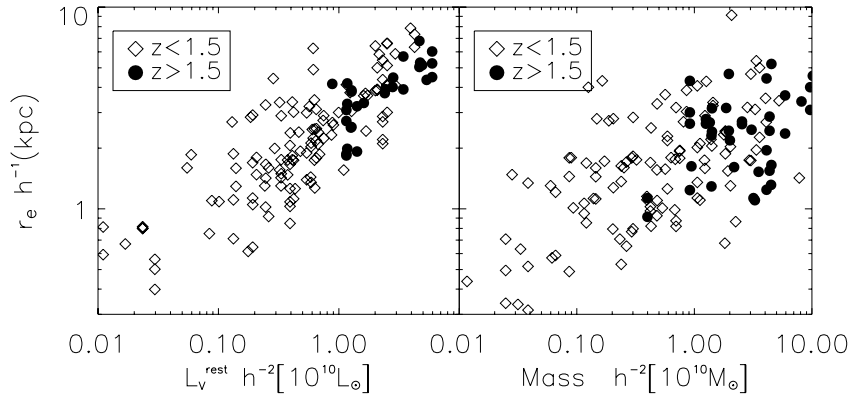

FIG. 11.—Predictions of the null hypothesis. *Left*: Simulated distribution of rest-frame optical sizes vs. the rest-frame *V*-band luminosities for the SDSS data (see text for details). Galaxies with redshifts smaller than 1.5 are shown by open diamonds and galaxies with redshifts bigger than 1.5 by filled circles. *Right*: Same as in the left panel, but with the stellar mass.

TABLE 2
PROPERTIES OF THE BIN SELECTION

L_V ($10^{10}\ h^{-2}\ L_\odot$) (1)	$\bar{r}_e(L,\ 0)$ (h^{-1} kpc) (2)	$\sigma(L,\ 0)$ (h^{-1} kpc) (3)	z' (4)	$\bar{r}_e(L, z = 2.5)/\bar{r}_e(L,\ 0)$ (5)
3–10	6.45	0.36	3.91	0.25(±0.10)
1–3	3.68	0.33	2.58	0.35(±0.10)
0.3–1	2.07	0.40	1.55	...
M_* ($10^{10}\ h^{-2}\ M_\odot$)	$\bar{r}_e(M_*,\ 0)$ (h^{-1} kpc)	$\sigma(M_*,\ 0)$ (h^{-1} kpc)	z'	$\bar{r}_e(M_*, z = 2.5)/\bar{r}_e(M_*,\ 0)$
3–10	2.46	0.44	3.17	0.60(±0.15)
1–3	1.94	0.49	2.52	0.80(±0.20)
0.3–1	1.70	0.52	1.70	...

NOTES.—Properties of the bin selection for analyzing the evolution of sizes in the FIRES data. Col. (1): The luminosity (mass) range of the bin. Col. (2): SDSS mean size at $z \sim 0$ of galaxies with a luminosity (mass) equal to the mean luminosity (mass) of the FIRES galaxies in the luminosity (mass) range of col. (1). Col. (3): Same as in col. (2), but with the SDSS dispersion. Col. (4): Largest observable redshift (for galaxies with $K_s < 23.5$) for the mean luminosity (mass) of the analyzed bin. Col. (5): Implied size evolution at $z = 2.5$ according to our analysis (see text for details).

three subsamples. For the sizes at a given stellar mass the picture is qualitatively different: there is no evidence for significant evolution of the r_e-M_* relation, except for the most massive bin, $M_* > 3 \times 10^{10}\ h^{-2}\ M_\odot$. At $\langle M_* \rangle \sim 2 \times 10^{10}\ h^{-2}\ M_\odot$ the relation may only have changed by 20% since $z \sim 2.5$. The implied size evolution at $z = 2.5$ in each luminosity (mass) bin is summarized in Table 2. Note that in all cases the evidence for an evolving scatter of the L_V-r_e and M_*-r_e relations is marginal.

In Figure 13 we visualize these results in a different way: we show the ratio between the present-epoch mean size for every luminosity (mass) bin and the expected mean size as a function of redshift using the α-values derived from the FIRES data [i.e., we show $\bar{r}_e(L,z)/\bar{r}_e(L,\ 0) = (1+z)^{-\alpha}$]. The same is done for the mass. This figure shows the region enclosed by the 1 σ level confidence contours. The lines stop at the limiting redshift z' we are able to explore for the different luminosity (mass) bins.

Again, Figure 13 shows that high-z galaxies (most luminous bin) at $z \sim 2.5$ are more compact (a factor of 4) than the nearby equally luminous galaxies. On the other hand, high-z galaxies differ only slightly in size at a given mass from the present epoch. In the middle luminosity (mass) bin the

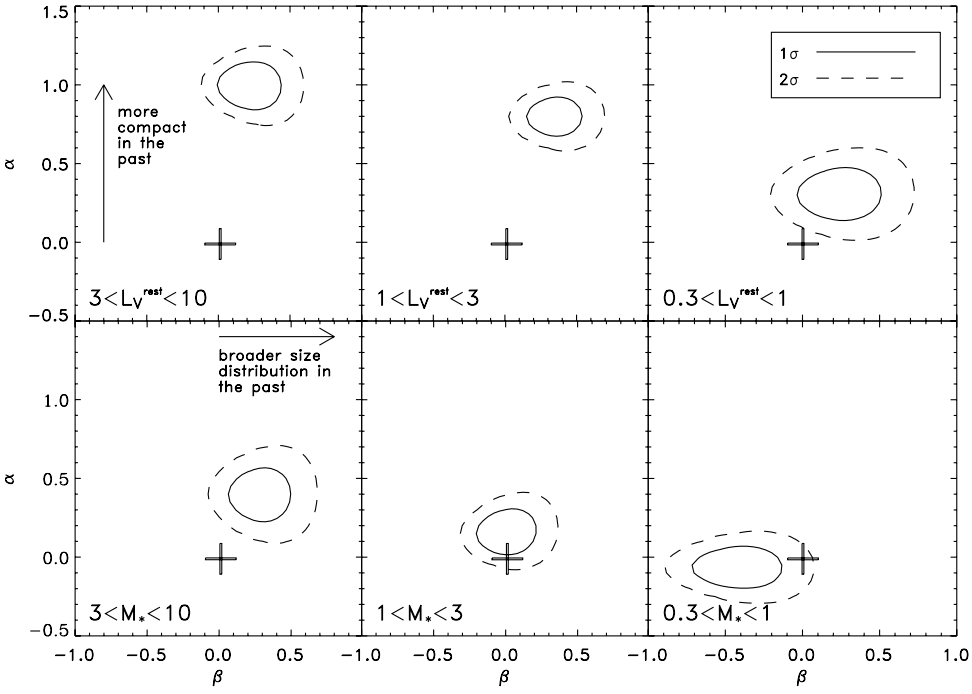

FIG. 12.—Likelihood contours representing the evolution in size and dispersion in the α-β plane. The top (bottom) panels show the evolution of the luminosity-size (mass-size) relation. The solid line represents the 1 σ confidence level contour, the dashed line the 2 σ confidence level. The cross shows the position of no evolution in this plane. Positive values of α represent decreasing values of the size with redshift. Positive values of β represent increasing the intrinsic dispersion σ of the population with redshift. Both the luminosity and the mass are in units of 10^{10} solar value. Both the no-evolution model and a luminosity-independent evolution model are less likely than the luminosity-dependent model.

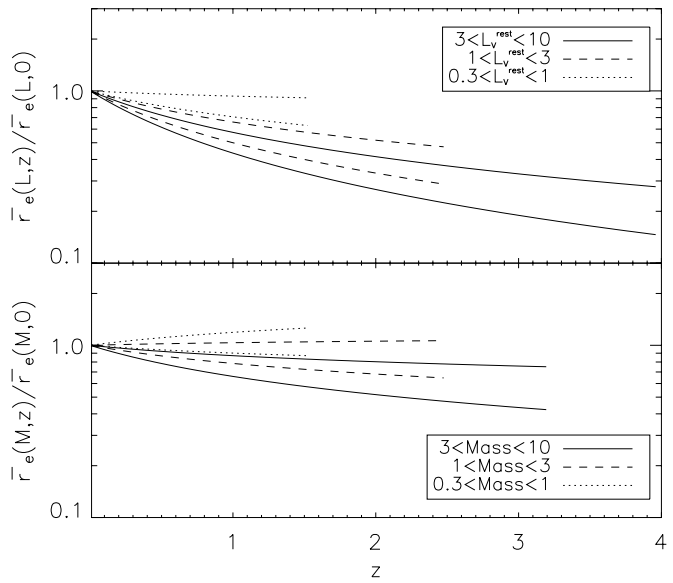

FIG. 13.—Ratio between the SDSS mean size and the expected mean size as a function of z shown for both the luminosity and mass relations. Both the luminosity and the mass are in units of 10^{10} solar value. Equal style lines enclose the 1 σ variation.

evolution with z appears to be less important. For the L_V-r_e relations the dispersion of the high-z population increases in all the cases. This increase is, however, relatively moderate (a factor of 1.2–2). We discuss how we can understand these results in the following section.

5. DISCUSSION

Using the observed nearby SDSS size relations (Shen et al. 2003) as the correct local references, the observed FIRES size-luminosity and mass-size distributions at high z show a very different degree of evolution. The mass-size relation has remained practically unchanged, whereas the size-luminosity relation has evolved significantly: there are many more compact luminous objects at high z than now. How can we reconcile these two observational facts?

In absence of M/L evolution with time, a change in the size-luminosity relation with z would imply the same degree of evolution in the mass-size relation. However, the mean M/L decreases with increasing z. In the nearby universe, most galaxies have large M/L (see Fig. 14 of Kauffmann et al. 2003). In contrast, FIRES galaxies at $z > 2$, at all luminosities, have M/L of the order $\sim$1 (G. Rudnick et al. 2004, in preparation). Consequently, although we observe a strong evolution in the luminosity-size relation, the decrease of M/L avoids a significant change in the observed mass-size relation.

We can therefore characterize our observed high-z galaxy population as follows: small to medium-size objects (effective radius $\sim$1.5 h^{-1} kpc) not very massive ($\sim 3 \times 10^{10}\ h^{-2}\ M_{\odot}$) but often very luminous ($\sim 3 \times 10^{10}\ h^{-2}\ L_{\odot}$) in the V band. The above picture does not mean that large galaxies cannot be found at high z (Labbé et al. 2003b), but that they are relatively rare.

Traditionally the high-z population has been selected by the Lyman break selection technique (Steidel & Hamilton 1993) known to select luminous unobscured star-forming galaxies. However, dust-obscured or UV-faint galaxies may have been missed. The galaxies in FIRES are selected from very deep NIR K_s-band imaging and, consequently, are expected to be less affected by this problem and give a more complete mass census of the high-z universe. In fact, the population of galaxies under study consists in part of a red population (Franx et al. 2003), which would be largely missed by the Lyman break technique, but whose volume number density is estimated to be half that of LBGs at $z \sim 3$.

Hierarchical models for structure formation in a Λ-dominated universe predict that LBGs have typical half-light radii of $\sim 2\ h^{-1}$ kpc (Mo et al. 1999), in good agreement with the size of the galaxies we are measuring and the observed sizes for LBGs of other authors (Giavalisco et al. 1996; Lowenthal et al. 1997). Interestingly, other authors have observed LBGs using optical filters, and, consequently, these sizes are UV sizes. The fact that their measures and ours (which are in the optical rest frame) do not differ significantly could be evidence that the star formation of the LBGs is extended over the whole object.[16] In fact, if we select in our sample those galaxies with $L_V > 2 \times 10^{10}\ h^{-2}\ L_{\odot}$ and $z > 2.5$, one-half of this subsample would be considered as LBGs following the Madau et al. (1996) color criteria. We will explore the relation of UV and optical sizes in a forthcoming paper.

"High-redshift disks are predicted to be small and dense, and could plausibly merge together to form the observed population of elliptical galaxies" (Mo et al. 1999). We have made a simplistic comparison between the above prediction and our data in Figure 14. The lines represent the expected internal mass density M/r_e^3 of disks galaxies just formed at each redshift for three different values of the specific angular momentum. These lines are evaluated combining equations (4) and (12) of Mo et al. (1999) and assume a constant fraction of the mass of the halo that settles into the disk, $m_d = 0.05$, and a constant spin parameter of the halo, $\lambda = 0.05$. With these two assumptions the internal mass density increases with z as the square of the Hubble constant $H(z)$.

Galaxies more massive than $10^{10}\ M_{\odot}$ are observable over the complete range in redshift. The measured mean internal density for this galaxy population appears to evolve only slightly with z, in agreement with the lack of strong evolution in the size-mass relation. If all the galaxies present in Figure 14 were disks, their distribution would not be compatible with the theoretical expectation. However, we must take into account that we are observing a mix of galaxy types and not only disk galaxies. In order to address this point, we have made a visual galaxy classification of all the objects with $z < 1.5$ and mass larger than $10^{10}\ M_{\odot}$. We can do that because of the high resolution of the *HST* images in the I_{814}-band filter. This examination showed that the dense objects ($M/r_e^3 > 10^{10}\ M_{\odot}\ \mathrm{kpc}^{-3}$) with $z < 1.5$ appear to be all elliptical galaxies and that the late-type fraction appears to increase as one moves to lower density objects. Unfortunately, we cannot make a similar analysis for $z > 1.5$, and the question of whether the high-density objects we observe there are disk dominated remains unsolved. However, it is highly tempting to propose that our high-z dense population could be the progenitors of the nearby dense elliptical galaxies.

Independently of the nature of the LBGs and of the red population, it is clear that in order to reach the mass and sizes of the nearby galaxies, an evolutionary process must be acting on the high-z population. Recently, Shen et al. (2003) have proposed, for the early-type galaxies, a simple model of mass and size evolution based on subsequent major mergers. This

[16] There is some evidence that the LBG morphology depends not much on the wavelength, remaining essentially unchanged from the far-UV to the optical window (Giavalisco 2002 and references therein).

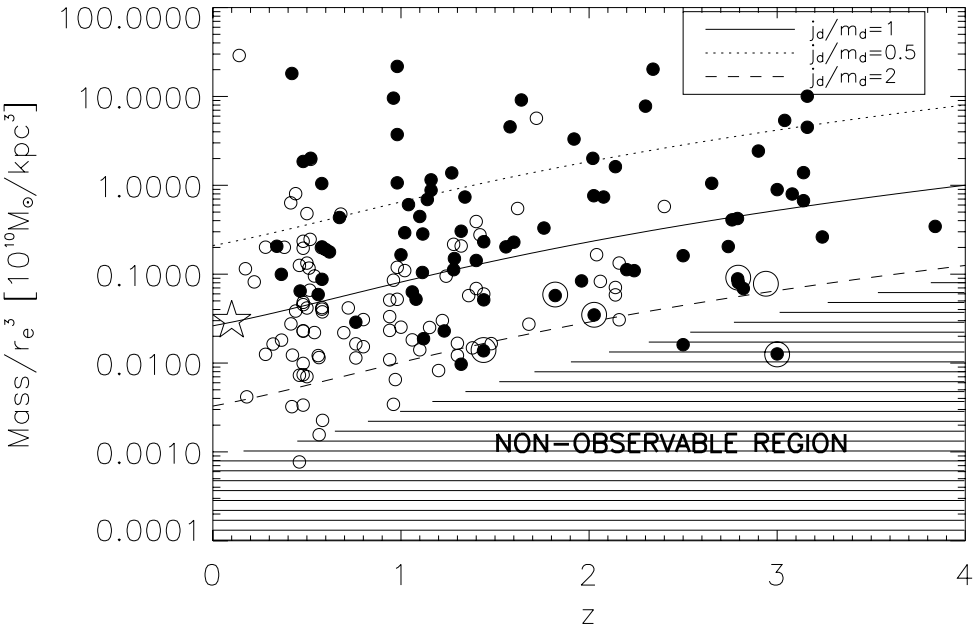

FIG. 14.—Internal density of the observed galaxies vs. z. In order to make a direct comparison with the theory expectation, we have used $h = 0.7$. Observed galaxies are separated into two groups: filled circles represent galaxies more massive than $10^{10}\ M_{\odot}$. These galaxies are observable over the full z range. The expected internal density M/r_e^3 of disk galaxies just formed at each redshift according to the Mo et al. (1999) model is shown for three different specific angular momentum j_d/m_d values. We have used $m_d = 0.05$ and $\lambda = 0.05$. The internal density of the Milky Way (*large open star*) is shown for comparison. In addition, we have encircled those galaxies proposed to be large disklike galaxies at high z following Labbé et al. (2003a). Note that there is a galaxy in the Labbé et al. (2003a) analysis that is not in our sample because it is outside of the field of view selected in this study.

model explains the observed relations for these kind of galaxies between mass and size in the SDSS data, i.e., $R \propto M^{0.56}$. In the Shen et al. (2003) picture two galaxies with the same mass ($M_1 = M_2$) and radius ($R_1 = R_2$) merge, forming a new galaxy with mass $M = 2M_1$ and radius $R = 2^{0.56}R_1$. If this process is repeated p times, $M = 2^p M_1$ and $R = 2^{0.56p}R_1$. If we take a galaxy at $z = 3$ (following our mass and size estimates) with $M_1 = 3 \times 10^{10}\ h^{-2}\ M_{\odot}$ and $R_1 = 1.5\ h^{-1}$ kpc, this implies that after three major mergers $M = 24 \times 10^{10}\ h^{-2}\ M_{\odot}$ and $R = 4.8\ h^{-1}$ kpc, in excellent agreement with the values we see in nearby galaxies ($M = 24 \times 10^{10}\ h^{-2}\ M_{\odot}$ and $R = 5\ h^{-1}$ kpc; see Fig. 10). These numbers may suggest that the massive and dense high-z population can be understood as the progenitors of the bright and massive nearby early-type galaxies.

6. SUMMARY

Using ultradeep NIR images of the HDF-S, we have analyzed the rest-frame optical band sizes of a sample of galaxies selected down to $K_s = 23.5$. This has allowed us to measure the evolution of the luminosity-size and mass-size relations out to $z \sim 3$. This is the first time that the rest-frame V-band sizes of such distant galaxies have been systematically analyzed as a function of stellar luminosity and stellar mass.

We compared our observed luminosity-size and mass-size relations to those measured in the nearby universe by the SDSS data (Shen et al. 2003). For this comparison we have analyzed in detail the detectability effects that high-z observations impose on the observed relations. From this comparison, assuming that the Shen et al. (2003) distributions are correct, we found the following:

1. The size-luminosity relation has evolved since $z \sim 2.5$. Luminous objects ($L_V \sim 3 \times 10^{10}\ h^{-2}\ L_{\odot}$) at $z \sim 2.5$ are 4 times smaller than equally luminous galaxies today.

2. The size–stellar mass relation has remained nearly constant since $z \sim 2.5$: for $\langle M_* \rangle \sim 2 \times 10^{10}\ h^{-2}\ M_{\odot}$ the change is 20% (±20%); for stellar masses larger than $3 \times 10^{10}\ h^{-2}\ M_{\odot}$ the characteristic mean size change is 40% (±15%).

The above results are reconciled by the fact that the M/L values of high-z galaxies are lower than nowadays $\langle M/L \rangle \sim 1$ (G. Rudnick et al. 2004, in preparation). Consequently, the brightest high-z galaxies are a group composed of a high internal luminosity density population but with a mean internal stellar mass density not much higher than found in the nearby universe. The observed small sizes of distant galaxies found here and in previous studies for LBGs (Giavalisco et al. 1996; Lowenthal et al. 1997; Ferguson et al. 2004) are in agreement with the small evolution of the mass-size relation because the typical masses of $z = 3$ galaxies are substantially smaller than those at low redshift.

We are happy to thank Shiyin Shen for providing us with the Sloan Digital Sky Survey data used in this paper and Boris Häussler for running GALFIT. We thank the staff at ESO for the assistance in obtaining the FIRES data and the Lorentz Center for its hospitality and support. We also thank the anonymous referee for useful comments.

Funding for the creation and distribution of the SDSS Archive has been provided by the Alfred P. Sloan Foundation, the Participating Institutions, the National Aeronautics and Space Administration, the National Science Foundation, the US Department of Energy, the Japanese Monbukagakusho, and the Max-Planck Society. The SDSS Web site is http://www.sdss.org. The SDSS is managed by the Astrophysical Research Consortium (ARC) for the Participating Institutions. The

Participating Institutions are the University of Chicago, Fermilab, the Institute for Advanced Study, the Japan Participation Group, Johns Hopkins University, Los Alamos National Laboratory, the Max-Planck-Institut für Astronomie (MPIA), the Max-Planck-Institut für Astrophysik (MPA), New Mexico State University, the University of Pittsburgh, Princeton University, the US Naval Observatory, and the University of Washington.

REFERENCES

Aguerri, J. A. L., & Trujillo, I. 2002, MNRAS, 333, 633
Avila-Reese, V., & Firmani, C. 2001, Rev. Mexicana Astron. Astrofis. Ser. Conf., 10, 97
Baugh, C. M., Cole, S., Frenk, C. S., & Lacey, C. G. 1998, ApJ, 498, 504
Bell, E. F., & de Jong, R. S. 2001, ApJ, 550, 212
Blanton, M., et al. 2003, ApJ, 592, 819
Casertano, S., Ratnatunga, K. U., Griffiths, R. E., Im, M., Neuschaefer, L. W., Ostrander, E. J., & Windhorst, R. A. 1995, ApJ, 453, 599
Casertano, S., et al. 2000, AJ, 120, 2747
Fasano, G., & Franceschini, A. 1987, MNRAS, 225, 155
Ferguson, H. C., et al. 2004, ApJ, 600, L107
Franx, M., et al. 2000, Messenger, 99, 20
———. 2003, ApJ, 587, L79
Giavalisco, M. 2002, ARA&A, 40, 579
Giavalisco, M., Steidel, C. C., & Macchetto, F. D. 1996, ApJ, 470, 189
Kauffmann, G., et al. 2003, MNRAS, 341, 33
Kroupa, P. 2001, MNRAS, 322, 231
Labbé, I. F. L., et al. 2003a, AJ, 125, 1107
———. 2003b, ApJ, 591, L95
Lilly, S., et al. 1998, ApJ, 500, 75
Lowenthal, J. D., et al. 1997, ApJ, 481, 673
Madau, P., Ferguson, H. C., Dickinson, M. E., Giavalisco, M., Steidel, C. C., & Fruchter, A. 1996, MNRAS, 283, 1388
Mao, S., Mo, H. J., & White, S. D. M. 1998, MNRAS, 297, L71
Mo, H. J., Mao, S., & White, S. D. M. 1999, MNRAS, 304, 175
Moorwood, A. F. 1997, Proc. SPIE, 2871, 1146
Peng, C. Y., Ho, L. C., Impey, C. D., & Rix, H. W. 2002, AJ, 124, 266
Press, W. H., Teukolsky, S. A., Vetterling, W. T., & Flannery, B. P. 1992, Numerical Recipes (Cambridge: Cambridge Univ. Press)
Roche, N., Ratnatunga, K., Griffiths, R. E., Im, M., & Naim, A. 1998, MNRAS, 293, 157
Rudnick, G., et al. 2001, AJ, 122, 2205
———. 2003, ApJ, 599, 847
Saglia, R. P., Bertschinger, E., Baggley, G., Burstein, D., Colless, M., Davies, R. L., McMahan, R. K., & Wegner, G. 1997, ApJS, 109, 79
Sérsic, J.-L. 1968, Atlas de Galaxias Australes (Cordoba: Observatorio Astronomico)
Shen, S., Mo, H. J., White, S. D. M., Blanton, M. R., Kauffmann, G., Voges, W., Brinkmann, J., & Csabai, I. 2003, MNRAS, 343, 978
Smail, I., Hogg, D. W., Yan, L., & Cohen, J. G. 1995, ApJ, 449, L105
Somerville, R. S., Primack, J. R., & Faber, S. M. 2001, MNRAS, 320, 504
Steidel, C. C., Giavalisco, M., Pettini, M., Dickinson, M., & Adelberger, K. L. 1996, ApJ, 462, L17
Steidel, C. C., & Hamilton, D. 1993, AJ, 105, 2017
Trujillo, I., Aguerri, J. A. L., Gutiérrez, C. M., & Cepa, J. 2001a, AJ, 122, 38
Trujillo, I., Graham, A. W., & Caon, N. 2001b, MNRAS, 326, 869
York, D., et al. 2000, AJ, 120, 1579